Nanoscale Horizons

ROYAL SOCIETY OF CHEMISTRY

COMMUNICATION

View Article Online
View Journal | View Issue

Cite this: *Nanoscale Horiz.*, 2022, 7, 1501

Received 26th July 2022,
Accepted 27th September 2022

DOI: 10.1039/d2nh00349j

rsc.li/nanoscale-horizons

In situ crafting of a 3D N-doped carbon/defect-rich $V_2O_{5-x}{\cdot}nH_2O$ nanosheet composite for high performance fibrous flexible Zn-ion batteries†

Rui Pan,[a] Anqi Zheng,[a] Bing He,[c] Yuwei Xiong,[a] Fengsai Han,[b] Lei Wei,[c] Qingwen Li,*[b] Qichong Zhang,*[b] Kuibo Yin*[a] and Litao Sun*[a]

Aqueous fibrous batteries with tiny volume, light weight and stretchability have furthered wearable smart textile systems like biocompatible electronics for a more efficient use of electricity. Challenges still faced by fibrous batteries include not only the deficient actual capacity but the cyclability on the cathode side. Herein, an *in situ* anodic oxidation strategy is reported to prepare 3D N-doped/defect-rich $V_2O_{5-x}{\cdot}nH_2O$ nanosheets (DVOH@NC) as fibrous cathodes for aqueous zinc-ion batteries (AZIBs). Benefiting from the substantially abundant reaction sites, enhanced electrical conductivity, short electron/ion diffusion path and high mass loading, the newly designed DVOH@NC fibrous electrode delivers impressive capacity (711.9 mA h cm^{-3} at 0.3 A cm^{-3}) and long-term durability (95.5% capacity retention after 3000 cycles), substantially outperforming previously reported fibrous vanadium-based cathodes. First-principles density functional theory (DFT) calculations further revealed that the oxygen vacancies can weaken the electrostatic interaction between Zn^{2+} and the host cathode accompanying the low Zn^{2+} diffusion energy barrier. To highlight the potential applications, a prototype wearable fiber-shaped AZIB (FAZIB) with remarkable flexibility and extraordinary weaving capability was demonstrated. More encouragingly, the resulting FAZIB could be charged with solar cells and power a pressure sensor. Thus, our work provides a promising strategy to rationally construct high-performance flexible vanadium-based cathodes for next-generation wearable AZIBs.

New concepts

Vanadium-based compounds for flexible and wearable aqueous zinc-ion batteries have emerged as a research hotspot recently, although the unsatisfactory capacity and cyclability have hindered the progress of rational cathode design thus far. In this work, fundamental insights gleaned from electrochemistry, theoretical calculations and mechanism characterization are employed to elucidate the role of vacancies and 3D geometric promotion in the electrochemical performance and electronic structure of $V_2O_{5-x}{\cdot}nH_2O$/N-doped carbon. Compared with V_2O_5/N-doped carbon which exhibits sluggish reaction kinetics, such a "conductive electrode" with enhanced electronic conductivity endows redox systems with much faster ion diffusion kinetics and offers an outstanding capability and long lifespan for $V_2O_{5-x}{\cdot}nH_2O$/N-doped carbon. Considering the potential tunability of multiple-oxidation-state vanadium oxide, this progress in flexible zinc aqueous batteries will be attractive for high-performance wearable electronics and devices.

Introduction

Researchers have recently witnessed a spike in the use of fibrous batteries with high performance and the ability to stretch/bend as a basis for developing biocompatible electronics, such as wearable sensors and soft actuators for monitoring health. Safety hazards of lithium-ion batteries (LIBs) including catching fire or even explosions and finite lithium reserves still pose dilemmas for flexible applications.[1–3] As compared to single-valent organic systems, multivalent aqueous chemistry, such as Al^{3+}, Mg^{2+}, Ca^{2+}, Zn^{2+}, *etc.*, is gifted with a more competitive energy density, abundant resources, and fewer safety concerns.[4–8] In particular, aqueous zinc ion batteries (AZIBs) have drawn considerable attention because of their appealing capacity (5851 mA h cm^{-3}), relatively high redox potential (−0.76 V *vs.* NHE), ease of manufacture, and rich natural storage.[9] Besides, fibrous electrodes based on conductive carbon nanotube fibers (CNTFs) with exceptional flexibility and weavability have broadened their applications even to the military area.[10] However, to date only limited fiber-shaped AZIBs (FAZIBs) are available due to the lack of corresponding high-performance fiber electrodes, and there continues

[a] *SEU-FEI Nano-Pico Center, Key Laboratory of MEMS of Ministry of Education, Southeast University, Nanjing, 210096, China. E-mail: yinkuibo@seu.edu.cn, slt@seu.edu.cn*

[b] *Key Laboratory of Multifunctional Nanomaterials and Smart Systems, Suzhou Institute of Nano-Tech and Nano-Bionics, Chinese Academy of Sciences, Suzhou 215123, China. E-mail: qwli2007@sinano.ac.cn, qczhang2016@sinano.ac.cn*

[c] *School of Electrical and Electronic Engineering, Nanyang Technological University, 50 Nanyang Avenue, 639798, Singapore*

† Electronic supplementary information (ESI) available. See DOI: https://doi.org/10.1039/d2nh00349j

to be an enormous challenge in fabricating FAZIBs with promising life expectancy and appealing capability.

Among the new candidates for AZIB cathode materials, vanadium-based oxides are particularly attractive cathode materials for AZIBs owing to their high theoretical capacity, versatile crystal structures and multiple oxidation states of vanadium.[11,12] In practice, vanadium-based oxides are disadvantaged by low electronic conductivity and unstable structure, and thus often display limited capacity and low cycling stability.[13] To address this issue, extensive efforts have been devoted to developing vanadium-based oxide cathodes toward higher capacity and better cyclic stability, including the pre-insertion of cations and structural water to increase layer spacing and enhance reaction kinetics.[14–16] Despite the significant progress achieved, these vanadium-based oxide materials are primarily fabricated in various powder forms, and these common slurry-processed powder electrodes generally contain binders and additives, fundamentally eliminating some of the active sites and thus degrading the performance of the vanadium-based oxide materials.[17,18] Undoubtedly, developing binder-free electrodes would not only remove the undesirable interfaces generated by additional binders/conductive agents, but also provide a large specific surface area, rich reaction sites and short electron/ion diffusion path.[19,20] Hence, developing binder-free vanadium-based oxide electrodes has brought new insights into FAZIBs.

To date, it is extraordinarily difficult to fabricate vanadium-based oxide freestanding electrodes co-intercalated with cations and structural water molecules. However, pure vanadium-based oxides can easily be grown on various conductive substrates.[21] It is highly desirable to fabricate high capacity, high rate and long cycle life vanadium-based oxide freestanding electrodes. The *in situ* electrochemical oxidation strategy is a simple and effective strategy to prepare high-valence vanadium-based oxides by introducing oxygen-containing functional groups. Notably, the activation process could modify surface chemistry,[22] produce an abundance of active sites,[23] induce structure disorder,[24] and concomitantly generate lattice vacancies because of the charge compensation effect.[25,26] Under the condition of high constant potential, the electrode material will be oxidized and the conductivity of the electrode will be modified.[27,28] It remains challenging to develop vanadium-based oxide freestanding electrodes with high capacity and high conductivity by the *in situ* electrochemical oxidation strategy. According to the energy band theory, the energy band structure of metal oxides can be adjusted by defect engineering to make the valence band transition across the Fermi level and accordingly increase their electronic conductivity.[29,30] Note that constructing core–shell heterostructures is an effective way to improve the mass loading of active materials and increase the capacity accordingly.[31] Thus, the rational design of core–shell heterostructures with defect-rich vanadium-based oxides is necessary to develop high-performance cathode materials for AZIBs.

Herein, we demonstrated that defect-rich $V_2O_{5-x}{\cdot}nH_2O$ was supported on 3D N-doped carbon nanowall arrays as freestanding fibrous cathodes (DVOH@NC) *via* an *in situ* electrochemical oxidation strategy. N-doped carbon nanoarrays with superior electron conductivity can enlarge the surface area of carbon nanotube fibers (CNTFs) and the mass loading of the active material. Meanwhile, first-principles density functional theory (DFT) calculations proved that the oxygen-defect engineering weakens the electrostatic interaction and reduces the Zn^{2+} diffusion energy barrier, hence boosting rapid Zn^{2+} insertion/extraction and suppressing cathode dissolution. Impressively, DVOH@NC delivers a high capacity of 711.9 mA h cm^{-3} at 0.3 A cm^{-3} and even retains 98.5% of its capacity after 200 cycles at 0.6 A cm^{-3}. Simultaneously, an excellent capacity retention of 95.5% is observed after 3000 cycles at 30 A cm^{-3}. This work opens an efficient avenue for the rational design of freestanding vanadium-based oxide cathodes for wearable AZIBs.

Experimental section

Fabrication of VN@NC@CNTF

First, a mixture of 0.3 mL vanadium oxytriisopropoxide and 45 ml isopropanol with several NC@CNTFs immersed was sealed in an autoclave, and kept at 200 °C for 10 h. After that, the as-fabricated VO_x@NC/CNTF was annealed at 600 °C for 2 h in an NH_3/Ar (ratio = 1 : 1) atmosphere at 600 °C for 2 h to acquire vanadium nitride supported on NC@CNTF (VN@NC@CNTF).

Fabrication of DVOH@NC@CNTF

DVOH@NC@CNTF was prepared *via* an *in situ* anodic oxidation strategy. Typically, the ZIBs consisted of VN@NC@CNTF as the cathode, 3 M $Zn(CF_3SO_3)_2$ as the aqueous electrolyte, and Zn wire as the anode, and were charged to 2 V in their first cycle to activate the cathode material. VN@NC@CNTF underwent an irreversible phase transition into DVOH@NC@CNTF.

Assembly of wearable FAZIBs

Zn nanosheets were deposited onto CNTFs (Zn@CNTF) by a facile electrochemical deposition process at a negative current density of 10 mA cm^{-2} for 10 min in 40 ml electrolyte (5 g of zinc sulfate heptahydrate, 5 g of sodium sulfate, and 0.8 g of boric acid). A PVA–$Zn(CF_3SO_3)_2$ gel electrolyte was achieved by mixing 5 g of PVA and 18.2 g of $Zn(CF_3SO_3)_2$ in 50 ml of deionized water under vigorous stirring at 95 °C for 2 h. The as-fabricated DVOH@NC@CNTF and Zn@CNTF were then suspended in the PVA–$Zn(CF_3SO_3)_2$ gel electrolyte and dried at 60 °C in a vacuum for 2 h. Finally, the two electrodes with thin layer PVA–$Zn(CF_3SO_3)_2$ gel electrolyte were twisted together to obtain a wearable FAZIB. For comparison, VO@NC@CNTF, DVOH@CNTF and VO@CNTF coupled with Zn@CNTF to assemble wearable FAZIBs can be realized by a similar procedure.

Description of DFT calculations

As implemented in VASP, the PBE (Perdew–Burke–Ernzerhof) functional and projector-augmented wave (PAW) methods were used for DFT calculations. Taking into account the strong on-site Coulombic interactions of the V 3d electrons, the DFT+U method was adopted with U_{eff} = 4.2 eV to account for self-

interaction of the V d-electrons. The van der Waals interaction between layers and structural water was evaluated by the van der Waals-corrected D2 method of Grimme. The lattice structures were fully relaxed until the maximum energy difference and residual force on atoms reached 10^{-6} eV and 0.01 eV $Å^{-1}$, respectively. An energy cut-off of 500 eV was employed. A $1 \times 2 \times 1$ supercell was assumed to describe oxygen vacancies and the intercalation of Zn^{2+}, and the corresponding Monkhorst–Pack grids were $3 \times 5 \times 3$. By employing this scheme, metal–metal interactions can be overlooked at low intercalation concentrations, while the interaction between added Zn^{2+} and the bilayered host, $V_2O_5{\cdot}nH_2O$, can be studied. The diffusion of Zn^{2+} between $V_2O_5{\cdot}nH_2O$ layers was simulated using the CI-NEB method.

Results and discussion

The fabrication process of the DVOH@NC@CNTF cathode is schematically illustrated in Fig. 1a. Specifically, the method includes solvothermal precipitation synthesis, a post-annealing process and *in situ* electrooxidation reaction (see the experimental details in the ESI†). As can be observed in the low-magnification scanning electron microscope (SEM) image (Fig. 1b), the triangular Co-MOF was integrated on the CNTF with uniformity and density, while the high-magnification EDS elemental mapping in Fig. 1c and energy dispersive profile (Fig. S1, ESI†) confirmed homogenous elemental dispersion of C, N, and Co in Co-MOF. The X-ray diffraction (XRD) profile of Co-MOF@CNTF in Fig. S2 (ESI†) further verified the characteristic crystalline nature of the ZIF-L structure.[32] Then the as-fabricated Co-MOF@CNTF was calcined in H_2/Ar followed by wet etching chemistry to provide the porous conductive N-doped carbon nanowall skeleton (NC) (Fig. 1d), which enables an increased surface area of CNTF.[33] Thereafter, electrochemically active vanadium pentoxide was successfully deposited on the NC nanowall *via* solvothermal precipitation and crystallization in the air to form V_2O_5 supported on NC nanowall arrays (VO@NC). After the obtained VO@NC@CNTF underwent post-annealing in ammonia, well-defined core–shell VN nanosheets on NC nanowalls evenly distributed on CNTF (VN@NC@CNTF) can still be noted in Fig. 1e and f and Fig. S3 (ESI†), indicating the strong bonding between VN nanosheets and

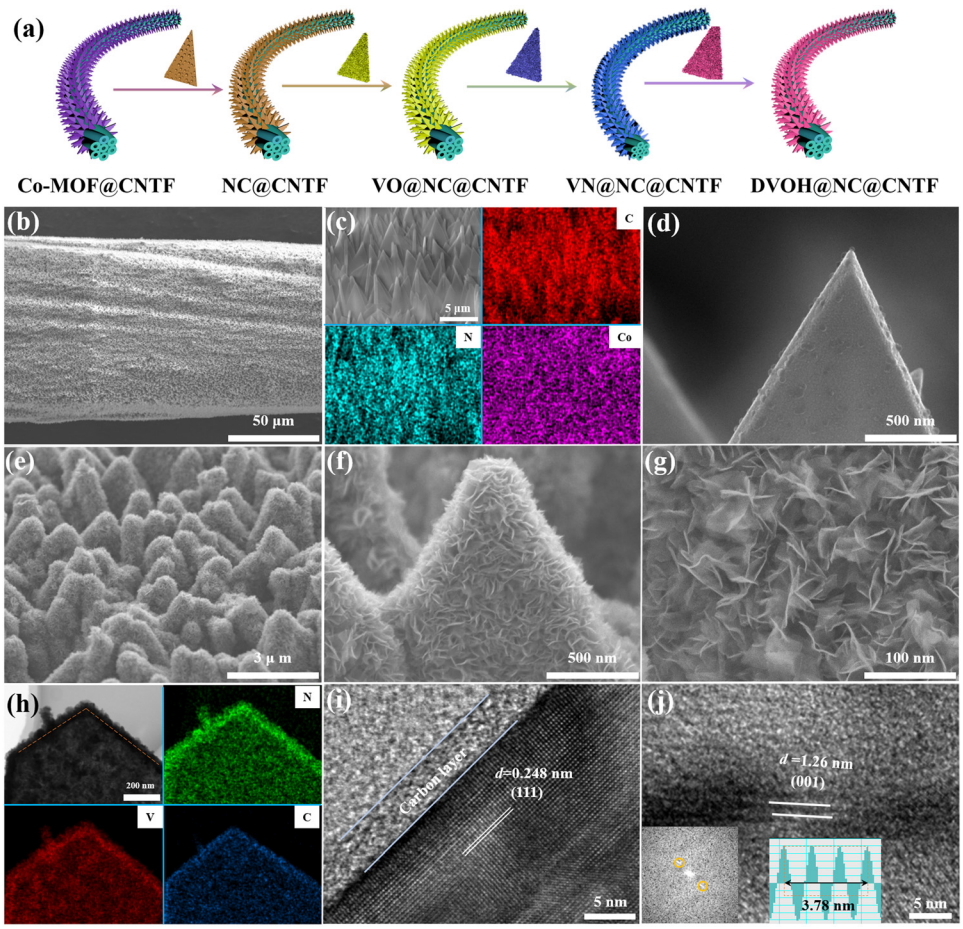

Fig. 1 (a) Schematic fabrication process of DVOH@NC@CNTF. (b and c) SEM images of Co-MOF anchored on CNTF and selected area of Co-MOF@CNTF with EDS elemental mapping. (d) NC nanowalls on CNTF. (e and f) SEM images of VN@NC heterostructures. (g) High-magnification SEM image of DVOH@NC@CNTF. (h) TEM image and corresponding EDS elemental dispersion images of core–shell VN@NC heterostructures. (i) High-magnification TEM image of the rock salt VN lattice. (j) Defective layered DVOH nanostructure.

the inner NC nanowalls. Subsequently, the VN@NC@CNTF was transformed into the final defect-rich $V_2O_{5-x}{\cdot}nH_2O$@NC@CNTF (DVOH@NC@CNTF) *via* an *in situ* electrooxidation activation process (Fig. 1g). During this process, a constant anodic current imposed on an AZIB system increased the valence of the V transition element in the electrode material, triggering an escape/encapsulation of the corresponding electronegative elements to compensate charge and releasing mechanical strain and stress.[23] The EDX mapping results of V, N and C evidently show that the VN@NC core–shell is constructed of outer VN nanosheets and inner N-doped triangle-shaped carbon nanowalls, respectively. Transmission electron microscopy (TEM) images provide further insight into the detailed structure of VN during the *in situ* anodic oxidation process. Fig. 1i shows that a lattice interplanar distance of 2.48 Å can be indexed to the (111) facet of the VN phase in the high-resolution TEM image.[34] After full activation under an anodic current, a new phase, with an unclear lattice fringe of 12.6 Å corresponding to (001) of $V_2O_5{\cdot}nH_2O$ (Fig. 1j), was noticed, and the unclearness of the lattice fringe may be caused by abundant defects/vacancies.[15,35–37] For comparison, VO@CNTF (Fig. S4, ESI†) and DVOH@CNTF samples without the N-doped carbon skeleton were also prepared by a similar method.

To further comprehend the mechanism of the *in situ* electrochemical activation during the first charging process, various characterization techniques were employed. As demonstrated in Fig. 2a and b, the small-angle X-ray scattering (GISAXS) pattern with diffraction rings showed the polycrystalline nature of the material. The scattering profiles are obtained from GISAXS by integrating the 2D mapping along the radial direction, where round rings represent isotropy in the scattering patterns. Fig. 2 demonstrates the crystalline nature of VN, in good agreement with cubic VN (JCPDS No. 35-768 ($Fm\bar{3}m$)).[38,39] After anodic oxidation, a brand-new broadened diffraction ring around the center construed as $V_2O_5{\cdot}H_2O$ with low crystallinity can be clearly observed; in contrast, the characteristic diffraction rings of VN nearly vanish.[40,41] The XRD result was suggestive of the effective electrochemical oxidation process and is consistent with the previous TEM analysis. These irreversible structure changes were further revealed by the Raman shift. As evidenced by Fig. 2c, the pristine VO@NC@CNTF cathode exhibits several typical V–O vibration peaks. The high-frequency peak (~995 cm^{-1}) belongs to

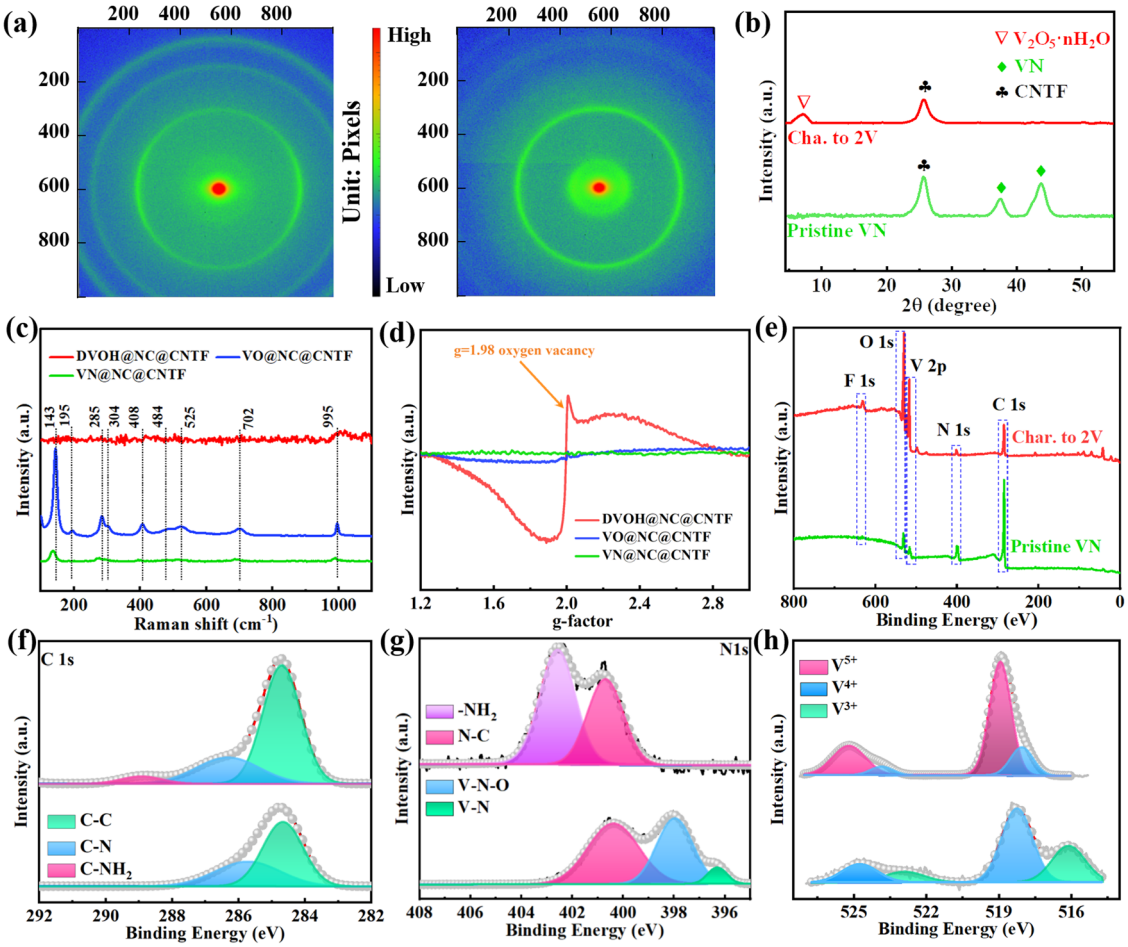

Fig. 2 (a) Transmission X-ray diffraction mapping of VN@NC@CNTF (left) and DVOH@NC@CNTF (right). (b) XRD spectra of VN@NC@CNTF and DVOH@NC@CNTF. (c) Raman shift and (d) EPR spectra of VN@NC@CNTF, DVOH@NC@CNTF and VO@NC@CNTF. (e) Full XPS spectra and (f) C 1s, (g) N 1s and (h) V 2p high-resolution spectra of VN@NC@CNTF and DVOH@NC@CNTF.

the stretching vibration of terminal unshared oxygen (V═O), with the bending mode of V═O sitting at around 408 and 285 cm^{-1}. Besides, the stretching and bending modes for doubly coordinated oxygen (V_2–O) can be correspondingly identified at 484 and 702 cm^{-1}. Similarly, the peaks located at 525 and 304 cm^{-1} were in correspondence with the stretching and bending vibrations of triply coordinated oxygen (V_3–O). While those at low frequency (143 and 195 cm^{-1}) originated from the lattice vibration.[42,43] In contrast with VO@NC@CNTF, blue shift of the VN@NC@CNTF vibration peaks (~10 cm^{-1}) towards lower wavenumbers and decreased peak intensity were observed, implying the successful replacement of lattice O of vanadium pentoxide with N atoms from ammonia to synthesize vanadium nitride.[39,44] Notably, the anodic oxidation process of VN@NC@CNTF led to disappearance of most Raman vibration peaks except one at ~995 cm^{-1}, due to long-range structural disorder and ample lattice defects derived from the anion substitution in the VN lattice by O^{2-} anions in H_2O while the charge compensation takes effect.[45,46] Furthermore, electron paramagnetic resonance (EPR) spectra (Fig. 2d) were recorded to deliver direct evidence for the abundant oxygen defects (*g*-factor of 1.98) of DVOH@NC@CNTF introduced by anodic oxidation, which were suitable for fast Zn-ion insertion/extraction.[47] In addition, X-ray photoelectron spectroscopy (XPS) analysis signposted element variation and coordination environment before and after activation. Fig. 2e shows that VN@NC@CNTF contained the most nitrogen, and the oxidized product contained the highest proportion of oxygen element. As shown in Fig. 2f and g, the two convoluted peaks (~396.3 eV and ~397.8 eV) assigned to V–N and V–N–O in the N 1s XPS spectra were substantially decreased and a new peak at *ca.* 402.5 eV corresponding to the $-NH_2$ group emerged, while only a small bump at ~288.7 eV in the C 1s spectra appeared, indicating the dissolution of nitrides and absorption of $-NH_2$ species in the activation process. Fig. 2h demonstrates that the valence state of vanadium in VN (V^{4+}/V^{3+}) is increased to a higher state (V^{4+}/V^{5+}) during the activation. Besides, no Zn element was detected after the electrochemical activation process (Fig. S5, ESI†). Simultaneously, a decrease in pH value took place, as observed in Fig. S6 (ESI†). Based on the above-detailed discussion, the *in situ* anodic transformation process can probably be formulated below:

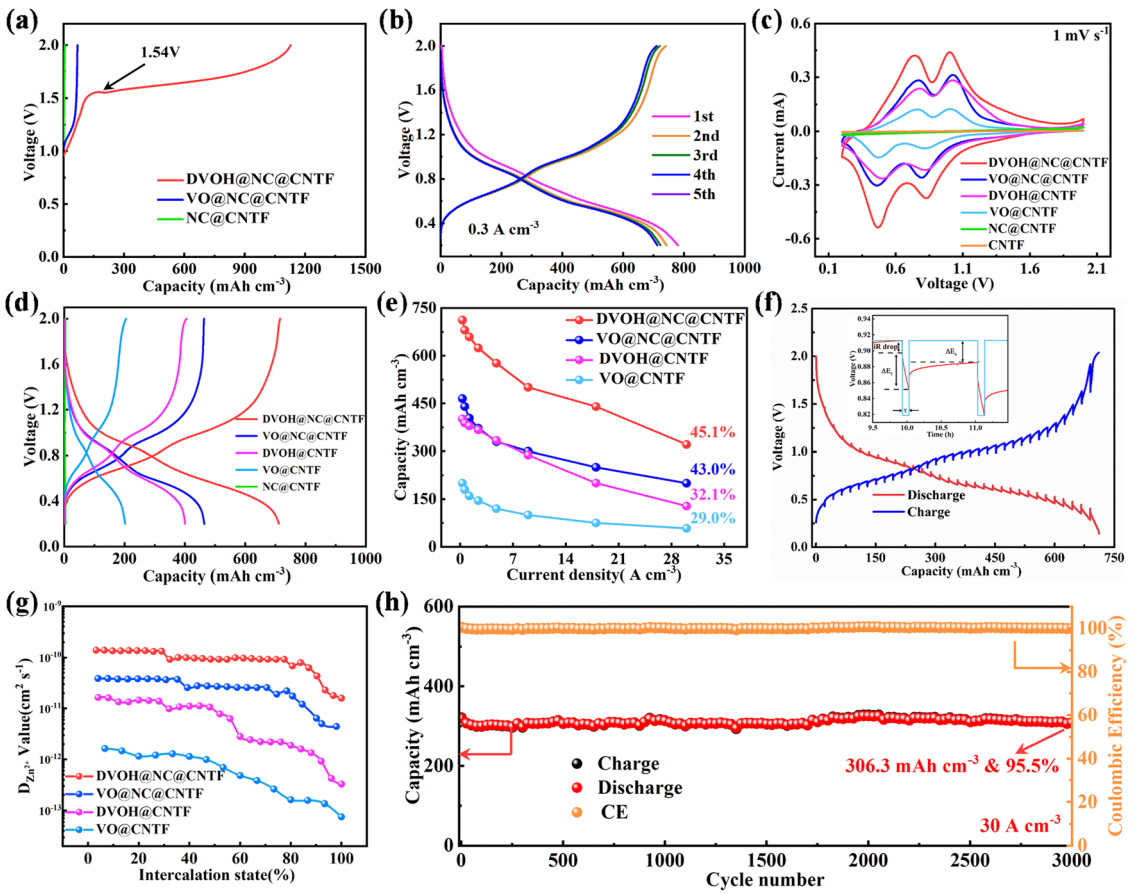

Fig. 3 (a) The *in situ* anodic oxidation curves of DVOH@NC@CNTF, VO@NC@CNTF and NC@CNTF. (b) First five cycles of GCD curves of DVOH@NC@CNTF. (c) CV and (d) GCD curve comparisons of DVOH@NC@CNTF, VO@NC@CNTF, DVOH@CNTF, VO@CNTF and NC@CNTF. (e) Capacity retention comparisons of DVOH@NC@CNTF, VO@NC@CNTF, DVOH@CNTF and VO@CNTF. (f) GITT curves of DVOH@NC@CNTF (Inset: selected steps during the discharging process.). (g) Zn ion diffusion coefficient comparison of DVOH@NC@CNTF, VO@NC@CNTF, DVOH@CNTF and VO@CNTF. (h) Cycling performance of the DVOH@NC@CNTF cathode at 30 A cm^{-3}.

$$2VN + (5 - x + n)H_2O - (4 - 2x)e^- = V_2O_{5-x}\cdot nH_2O + 2NH_4^+ + (2 - 2x)H^+ \quad (1)$$

To gain insight into the merits of oxygen defects and carbon matrix design, a series of electrochemical measurements were carried out for the DVOH@NC@CNTF, VO@NC@CNTF, DVOH@CNTF and VO@CNTF batteries paired with a Zn wire anode. Recent research work has revealed that *in situ* electrochemical oxidation strategies could induce phase transformation of low-valence vanadium-based compounds.[27,48] As confirmed in Fig. 3a, in contrast to the VN@NC@CNTF electrode, there is no voltage plateau for VO@NC@CNTF and NC@CNTF electrodes in the first charge profile, indicating the unchanged structure of VO@NC@CNTF and NC@CNTF. Remarkably, the CV (cyclic voltammetry) curves of the DVOH@NC@CNTF electrode exhibit two couples for typical redox peaks of vanadium-based oxides at approximately 0.50/0.81 V (V^{4+}/V^{3+}) and 0.87/1.03 V (V^{5+}/V^{4+}) (Fig. S7, ESI†), indicating a multistep reversible intercalation/de-intercalation of Zn ions.[49] As demonstrated in Fig. 3b, multiple redox couples occur in the GCD (galvanostatic charge/discharge) curves with two corresponding quasi-plateaus in the same potential window. It should be noted that the impressive reversibility and stability during repeated insertion and extraction of Zn ions can be reflected by the nearly coincident CV and GCD curves from the 2nd cycle. As is known to all, the 3D triangle-like morphology of the DVOH@NC composite can provide sufficient contact area between the electrolyte and electrode materials and enable a short zinc ion pathway. Meanwhile, the flexible and conductive medium NC@CNTF can enhance the conductivity of the cathode and improves the mass loading and conductivity of active materials. The integrated peak areas of the DVOH@NC@CNTF and VO@NC@CNTF from the CV curves in Fig. 3c are distinctly larger than those of DVOH@CNTF and VO@CNTF, implying that the construction of 3D NC nanosheets can lead to significant improvement of electrochemical performance. This is further confirmed by the corresponding GCD curves (Fig. 3d). Fig. 3e and Fig. S8a and b (ESI†) compare the rate performance profiles of DVOH@NC@CNTF, DVOH@CNTF, VO@NC@CNTF and VO@CNTF electrodes. Note that the rate capacity of DVOH@NC@CNTF substantially exceeded those of VO@NC@CNTF, DVOH@CNTF and VO@CNTF cathodes. Even at a much higher current density of 30 A m^{-3}, 45.1% (320.8 mA h cm^{-3}) of its initial capacity is still retained for the DVOH@NC@CNTF electrode, better than the VO@NC@CNTF (43.0%), DVOH@CNTF (32.1%) and VO@CNTF electrodes (29.0%), demonstrating its superior rate capability. When the current density was reset to 0.6 A cm^{-3}, the capacity of DVOH@NC@CNTF returned to the initial value, indicating the structural stability as well as rapid reaction kinetics of the electrode after various C-rate cycling. CV measurements at different scan rates were applied to investigate the electrochemical kinetics of the four cathodes, whose capacitive charge storage contributions are crucial for excellent electrochemical performance especially under high rates.[50] As seen in Fig. S8c (ESI†), the shapes of the CV curves were well-retained with the scan rates continuously increasing from 0.2 to 1 mV s^{-1}, reflecting the good reversibility of the DVOH@NC@CNTF cathode. Generally, by deconvoluting the current at a specified potential in the CV curves, different charge storage processes (diffusion-controlled and capacitor-like processes) can be quantitatively determined according to $i(V) = k_1v + k_2v^{1/2}$, where k_1 is estimated to be the fraction of currents describing capacitor-like processes. For the DVOH@NC@CNTF cathode, the surface capacitive contribution gradually enhanced with the increased scan rate and accounted for 89.1% of the charge storage at 1 mV s^{-1} (Fig. S8d, ESI†). Such an excellent capacitive behavior mostly translated to rapid rate capability can also be verified from *b*-value analysis (Fig. S9, ESI†). The capacitive-controlled contribution ratios of the four FAZIBs are compared in Fig. S8e and S10–S12 (ESI†), among which the DVOH@NC@CNTF and DVOH@CNTF cathodes delivered evidently higher capacitive contribution ratios than their respective counterparts (VO@NC@CNTF and VO@CNTF), which principally arises from the weak electrostatic host–intercalant interaction contributed by oxygen defects. Simultaneously, a similar trend was also observed when the cathodes were supported on NC nanowall arrays, suggesting that the introduction of a three-dimensional conductive skeleton enables a highly efficient electron transmission capability. EIS (electrochemical impedance spectroscopy) was carried out to further investigate the kinetics of charge and ion transport of the as-fabricated vanadium-based electrodes. As depicted in Fig. S13 (ESI†), in comparison with DVOH@CNTF and VO@CNTF electrodes, the charge-transfer resistances of DVOH@NC@CNTF and VO@NC@CNTF electrodes decrease significantly due to the high electron conductivity of NC nanosheets. Impressively, a higher slope line of the DVOH@NC@CNTF electrode is clearly observed, thus evidencing enhanced ion diffusion rate after the *in situ* electrochemical oxidation process.[51,52] Additionally, GITT (galvanostatic intermittent titration measurement) was further utilized to evaluate the Zn ion diffusion coefficient (D_{Zn}) for the DVOH@NC@CNTF electrode (Fig. 3f and Fig. S14, ESI†). As displayed in Fig. 3g, the calculated D_{Zn} value of Zn/DVOH@NC@CNTF batteries is as high as 1.6×10^{-11} to 1.4×10^{-10} cm^2 s^{-1}, substantially higher than that of VO@NC@CNTF, DVOH@CNTF, and VO@CNTF. This difference is ascribed to the high electrical conductivity of NC nanosheets and the low intercalation energy barrier of defect engineering. Additionally, continuous cycle tests *via* (dis)charging with different constant current densities of 0.6 A cm^{-3} and 30 A cm^{-3} were conducted. Encouragingly, the capacity of our DVOH@NC@CNTF‖Zn@CNTF FAZIBs decreased by less than 2% of the initial value at the end of 210 cycles (0.6 A cm^{-3}) after undergoing ~10 activating cycles (Fig. S15, ESI†). And even when evaluated at a high current density of 30 A cm^{-3}, it can still sustain an inspiring capacity retention of 95.5% (~306.3 mA h cm^{-3}) after cycling for 3000 cycles with a low capacity decay rate of 0.0015% per cycle (Fig. 3h). By contrast, the cycling performances of FAZIBs with VO@NC@CNTF, DVOH@CNTF and VO@CNTF cathodes were much inferior to that of DVOH@NC@CNTF (Fig. S16–S18, ESI†). This demonstrates that the fast kinetics and structural stability of DVOH@NC@CNTF cathodes were attributed to the abundant oxygen defect engineering and high conductivity NC skeletons, which can better the electronic conductivity and effectively alleviate the electrostatic interaction as

compared to the pristine VOH@NC@CNTF, VO@NC@CNTF and VO@CNTF. As seen in Fig. S8f (ESI†), the Ragone plot showed the excellent energy and power density of DVOH@NC@CNTF compared to the other three cathodes. To better demonstrate the excellent performance of our designed DVOH@NC@CNTF cathodes, the stereogram of volume capacity, areal capacity, capacity retention, cycle number, and energy density is plotted in Fig. S19 (ESI†), with a comparison to the batteries adopting VO@NC@CNTF, DVOH@CNTF and VO@CNTF as cathodes. Therefore, these remarkable properties make self-standing DVOH@NC@CNTF a promising cathode candidate for next-generation wearable AZIBs.

To clarify the mechanism of zinc storage and the contribution of oxygen defects to the electronic structure in VOH and DVOH, DFT (density functional theory) calculations were performed. Fig. 4a depicts the optimized geometry configurations and the two-dimensional (2D) charge distribution of VOH and DVOH, in which the charge is uniformly distributed for perfect VOH while spare electrons visually accumulate around defect sites for the DVOH structure. Notably, these extra electrons, generated from extracting oxygen atoms from the VOH lattice, can delocalize the electron cloud of DVOH, thus resulting in increased capacity.[53,54] Moreover, the calculated DOS (density of states) and PDOS (projected density of states) of VO, VOH and DVOH are shown in Fig. 4b and Fig. S20 (ESI†). As a result of oxygen defect engineering, an apparent bandgap in the bare VO and VOH appears in the vicinity of the Fermi level and it disappears in the DVOH model. More importantly, the DOS across the Fermi level increases more for DVOH when compared with VO and VOH, confirming the improved electronic conductivity and enhanced reactivity for DVOH.[55] The charge difference calculated upon zinc ion insertion into VOH and DVOH is demonstrated in Fig. 4c. Electron dissipation from Zn to the V–O layer is observed in both structures, while the charge of Zn is partially delocalized to the surrounding V atoms near an oxygen vacancy in the case of the DVOH structure, further providing proof for the much more weakened Zn–O electrostatic interaction in DVOH with facilitated Zn desorption/adsorption capability compared to VOH. The CI-NEB (climbing image nudged elastic band) method is used for further comprehension of the decisive role of oxygen defects in imparting a lower diffusion barrier and increasing the mobility of Zn ions, as demonstrated in Fig. 4d. A drastically reduced diffusion energy barrier from 0.39 to 0.26 eV is exhibited for defective bilayer-VOH nanosheets, revealing significant promotion of the Zn ion diffusion kinetics, which is in good agreement with previous work.[56] These results provide strong evidence that the introduction of oxygen vacancies obviously lowers the diffusion resistance of Zn ions for DVOH, thus enhancing its conductivity of electrons (ions) and accordingly contributing to structural stability and superior electrochemical performance.

To better elucidate the mechanism of the battery, we used DVOH@NC@CNTF as a cathode material to fabricate a zinc ion

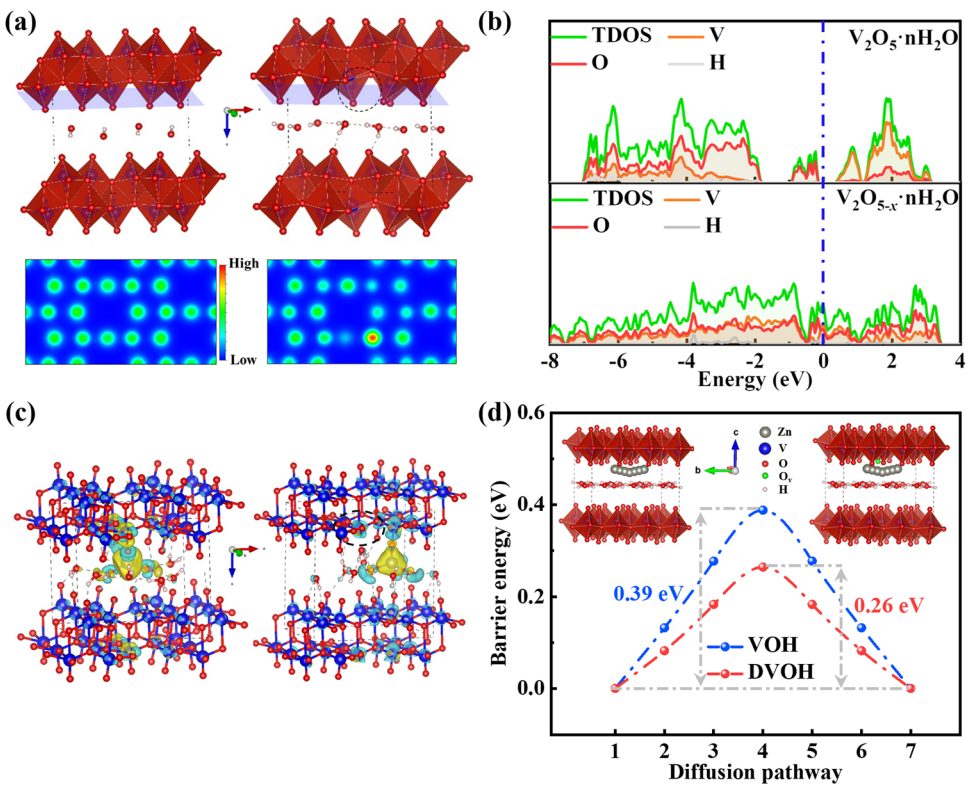

Fig. 4 (a) Optimized crystal structure of VOH and DVOH and corresponding charge distribution sliced along the (00*l*) direction. (b) Calculated DOS of the VOH and DVOH. (c) Charge density difference of the Zn/VOH and Zn/DVOH (yellow areas: electron depletion. Light blue areas: electron accumulation). The isosurface is set to be 0.005 e Å^{-3}. (d) Diffusion barrier profiles of Zn^{2+} transport in DVOH and VOH nanosheets along the *b* axis (insets show the Zn^{2+} diffusion process).

battery coupled with a Zn@CNTF anode in an aqueous 3 M $Zn(CF_3SO_3)_2$ electrolyte (Fig. 5a). First, *ex situ* XRD profiles at various charge/discharge states (selected points in Fig. 5b) were recorded to uncover the structural changes of DVOH@NC@CNTF in the second discharge/charge process (Fig. 5c). On discharging (a → d), the characteristic peak at ~7.5° assigned to the (001) diffraction of deficient $V_2O_5{\cdot}nH_2O$ exhibited a continuous slight shift towards lower angle accompanied by gradually decreased intensity, indicative of the gradual expansion of DVOH interlayer arrangements upon embedding zinc ions. A completely reverse progression taking place upon charging (d → g) meant a full recovery of the initial layered structure in a complete cycle, which is a benefit of the oxygen vacancy engineering of $V_2O_5{\cdot}nH_2O$ to weaken the electrostatic interaction between the zinc ions and the host cathode material as well as the increased electron conductivity caused by NC skeleton modification.[57,58] An in-depth analysis of the chemical compositions and coordination state variation during the discharge/charge process was then carried out by XPS. Fig. 5d illustrates the O 1s spectra with three fitted peaks, and the intensity of the shoulder peak at *ca.* 533 eV increased significantly upon discharge compared to the fully charged state, which can be assigned to the intercalated $[Zn(OH_2)_m]^{2+}$ or the absorbed H_2O molecules. Congruously, the highly reversible evolution of Zn 2p signals during the charge/discharge process in Fig. 5e suggests weaker interactions between inserted zinc ions and the V–O layers engineered by oxygen vacancies. In line with the DFT results, these oxygen vacancies contribute to a modest bonding rearrangement and less structural stress during (de)intercalation, permitting excellent rate capability and long-term cyclability. On top of that, V 2p XPS (Fig. 5f) evidenced reversible electrochemical oxidation/reduction of the V_2O_5 framework derived from Zn ion (de)intercalation. The V^{5+} peak ($2p_{3/2}$: 518.1 eV) dominated at the fully charged state, while the low valence V^{3+} ($2p_{3/2}$: 517.3 eV) component emerged with the intercalation of zinc ions. This is a fully reversible process where the high valence V^{5+} peak is

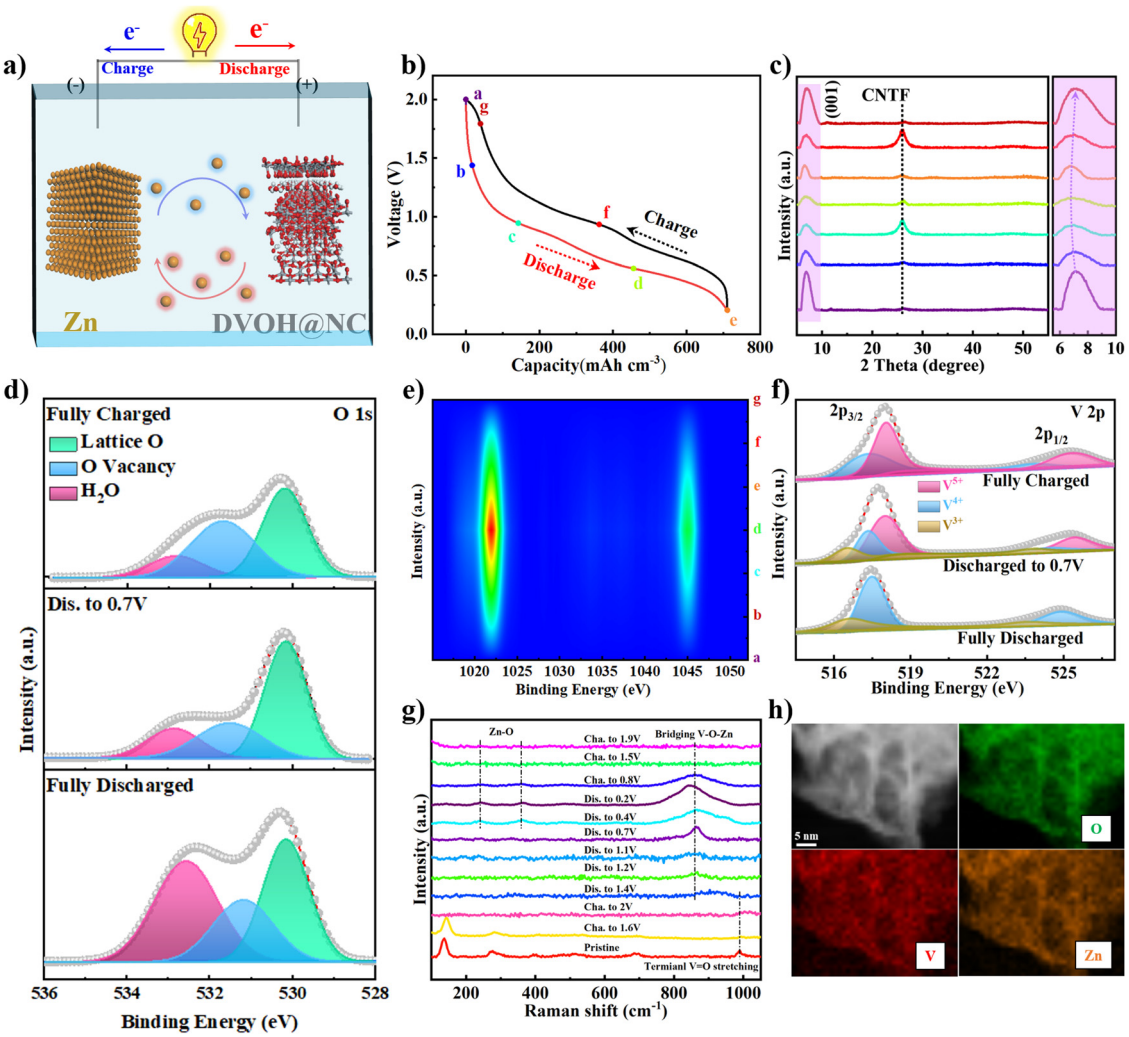

Fig. 5 (a) Schematic of the ion and electron transport behavior in the DVOH@NC@CNTF||Zn battery. (b and c) Various points in the second discharge/charge process for *ex situ* XRD tests. Fine XPS spectra of the material in different states of charge: (d) O 1s, (e) Zn 2p, and (f) V 2p. (g) *Ex situ* Raman spectra obtained during the charging/discharging processes. (h) TEM image of DVOH nanosheets and the corresponding elemental mappings of O, V, and Zn at the fully discharged state.

regenerated upon charging. *Ex situ* Raman measurements further substantiated the structure evolution of the DVOH@NC@CNTF electrode. As presented in Fig. 5g, all the vibration peaks gradually faded and even vanished on charging to 2 V, indicating the electrochemical transformation of VN@NC@CNTF to produce defect-rich DVOH@NC@CNTF. Upon discharging from 2 to 0.2 V, the intensity of a pair of Raman peaks at 250.2 and 353.1 cm^{-1} progressively strengthens, which stems from Zn–O vibrations, and another emerging peak at 862.3 cm^{-1} should be ascribed to the reordering of the V–O layers upon deep Zn ion insertion to form V–O–Zn bonds.[59] This reversible Zn–O bond formation evidencing the insertion/extraction of Zn ions in the defect-rich DVOH@NC@CNTF is also affirmed by TEM elemental mapping images of uniform distribution of O, V and Zn at the fully discharged/charged state (Fig. 5h and Fig. S21, ESI†).

As schematically illustrated in Fig. 6a, a quasi-solid state FAZIB can then be formed from the anode consisting of electrodeposited Zn nanosheets on CNTF (Zn@CNTF) (Fig. S22 and S23, ESI†) and the DVOH@NC@CNTF cathode with $Zn(CF_3SO_3)_2$–poly(vinyl alcohol) (PVA) as the gel electrolyte. Particularly, it is observed in Fig. 6b that the DVOH@NC@CNTF||Zn@CNTF FAZIBs can release reversible capacities of 402.6 mA h cm^{-3} at 0.03 A cm^{-3}, and still retain 40.6% of the original capacity level even at 30 A cm^{-3}, outperforming VOH@NC@CNTF||Zn@CNTF FAZIBs (Fig. S24, ESI†). CV measurements at various scan rates were then employed to investigate the electrochemical kinetics as capacitive charge storage contributions are vital for superior electrochemical performance. As seen in Fig. 6c, the shapes of the CV curves barely changed with the scan rates ranging from 0.2 to 1 mV s^{-1}, showing the good reversibility of DVOH@NC@CNTF||Zn@CNTF FAZIBs. Besides, the surface capacitive contribution gradually enhanced with the increased scan rate and accounted for 76.8% of the charge storage at 1 mV s^{-1} (Fig. 6d). The *b*-value analysis collected in Fig. 6e also shows that the two anodic peaks (O1 and O2) and cathodic peaks (R1 and R2) exhibit *b* values of 0.871, 0.839, 0.952 and 0.860 respectively, which reveals the excellent capacitive behavior. Such an excellent electrochemical performance mainly derives from the weak electrostatic host–intercalant interaction contributed by oxygen defects and the enhanced electron conductivity contributed by NC nanowall arrays. As seen in Fig. 6f, the Ragone plot showed that the energy and power densities of the DVOH@NC@CNTF||Zn@CNTF FAZIBs are substantially higher than those of previously reported fiber-shaped aqueous batteries and supercapacitors, highlighting the practical application of our FAZIBs over a wide range of power.[19,31,60–62]

To enhance the specific energy and power of the as-assembled FAZIBs for practical applications, we managed the operating current/voltage *via* serial/parallel integration strategies to achieve higher operating voltages and output currents. Extraordinarily, the output voltage and discharge time are doubled after connecting two FAZIBs in series and parallel as illustrated in Fig. 7a and b, thus demonstrating their excellent scalability. Moreover, a schematic diagram of some parameters is shown in Fig. 7c to assess the bending durability of FAZIBs, and the parameters included bending angle (θ), bending radius (R) and device length (L). Typically, when R and L are fixed, changing θ can result in different stressed areas, thus affecting the electrochemical performance of FAZIBs.[63,64] It is encouraging that the voltage curves of our FAZIBs under different bending angles were perfectly maintained (Fig. 7d). Even after continuous cycling tests at a current density of 2.4 A cm^{-3} at 30°, 60°, 90°, 120° and 180° bending angles, 97.4% of the specific capacitance (267.9 mA h cm^{-3}) is preserved, which

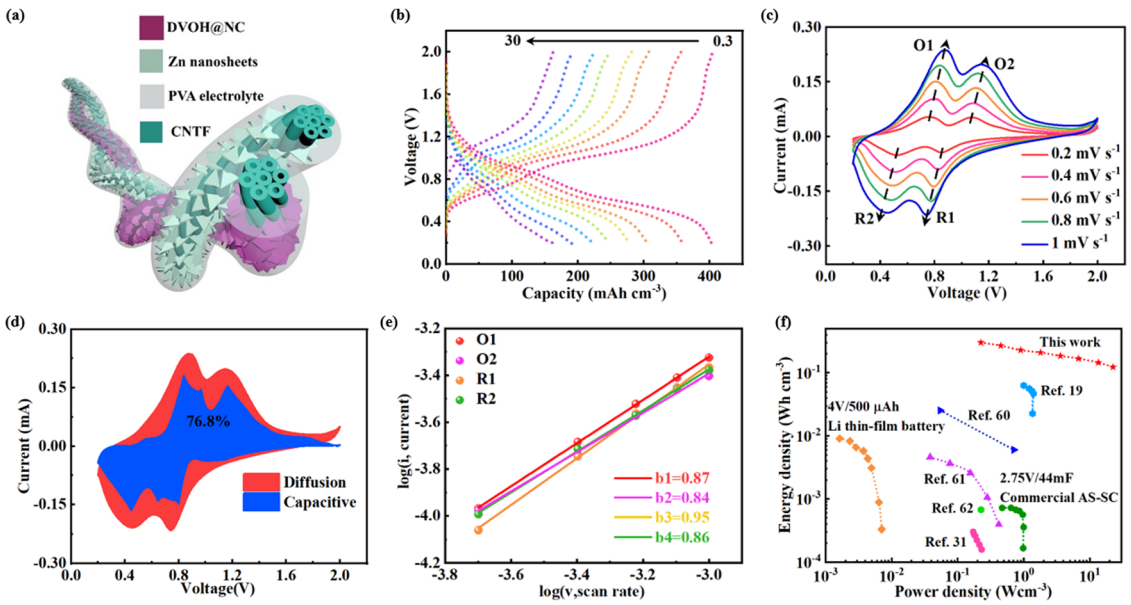

Fig. 6 (a) Schematic configuration of FAZIBs. (b) GCD curves at various current densities of DVOH@NC@CNTF||Zn@CNTF FAZIBs. (c) CV of DVOH@NC@CNTF||Zn@CNTF FAZIBs at different scan rates. (d) Capacitive and diffusion contributions to charge storage of DVOH@NC@CNTF||Zn@CNTF FAZIBs at 1 mV s^{-1}. (e) The calculated *b*-values from CV curves at different scan rates of DVOH@NC@CNTF||Zn@CNTF FAZIBs. (f) Ragone plot of our DVOH@NC@CNTF||Zn@CNTF FAZIBs and previously reported FAZIBs.

can be ascribed to the excellent mechanical properties of ultra-flexible CNTF and the strong adhesion of CNTF and active materials. In addition, a red light-emitting diode could be lit by two FAZIBs connected in series at 30° and 90° positions (Fig. S25 and S26, ESI†). To further evidence the practical applications of the newly developed FAZIBs as efficient devices for wearable energy storage components, these FAZIBs were weaved into fabrics as flexible power sources without detrimental damage to their performance (Fig. 7f). A solar rechargeable system (SRS) consisting of energy-harvesting solar cells and energy-storage components can efficiently convert and store intermittent solar irradiation. Herein, we fabricated a four-electrode solar-driven self-powered system to drive smart electronics, as illustrated in Fig. 7g. After fully discharging in the dark, the device is placed under light illumination for photo-charging at a constant charging rate (*i.e.* fixed area exposed to solar irradiation). The solar energy is stored in the FAZIBs in the form of chemical energy and can be converted into electrical energy at various current densities (Fig. 7h). Finally, another explored application for our deformable FAZIBs is powering a micro pressure sensor for real-time monitoring of subtle mechanical forces from wrist joint bending. As shown in Fig. 7j, the bending sensor could precisely capture and distinguish the joints at various bending angles (30° and 60°). Overall, these results demonstrated that our FAZIBs have great advantages for applications in wearable

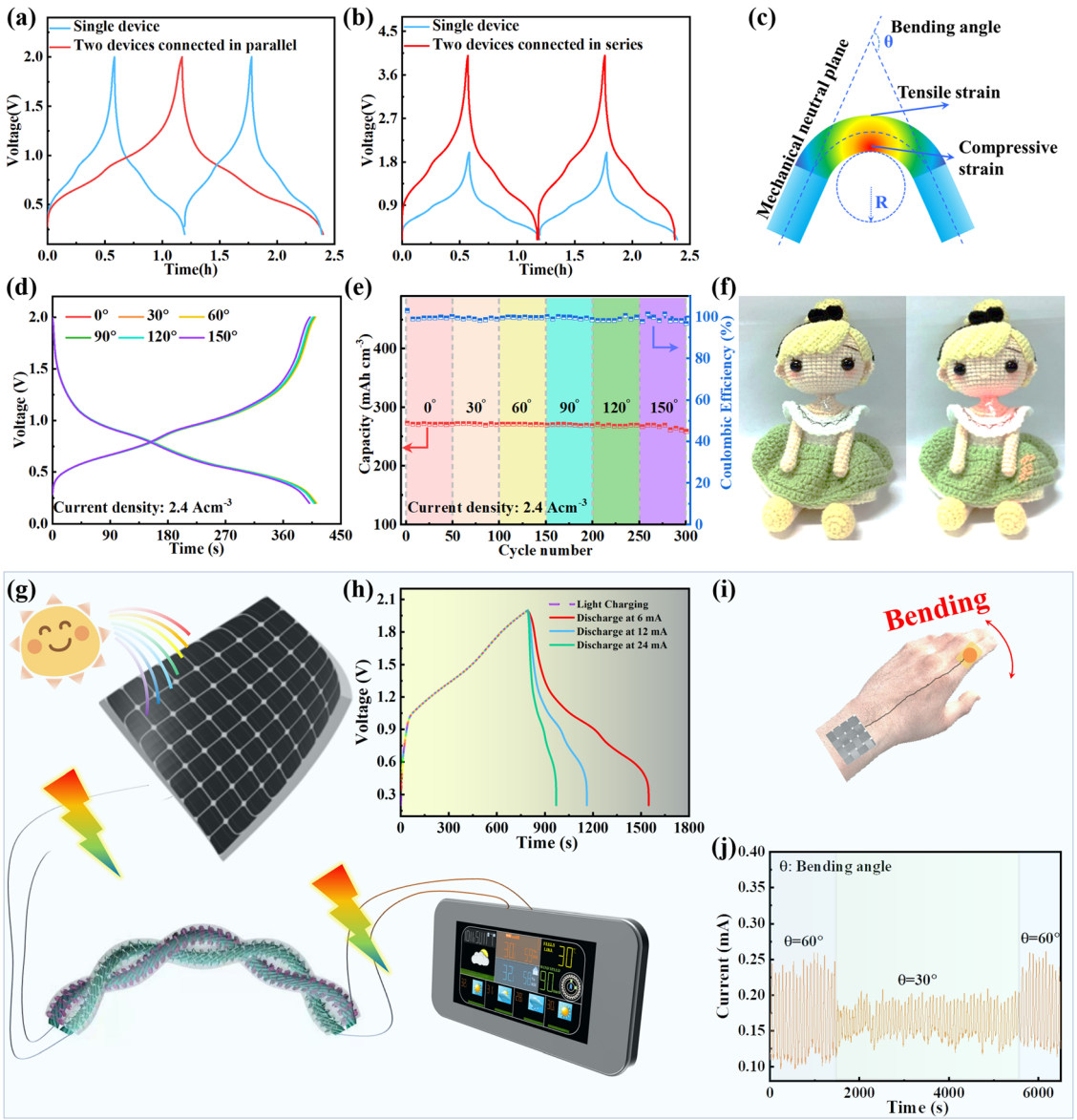

Fig. 7 GCD curves of two FAZIBs connected (a) in parallel and (b) in series. (c) Demonstration of different bending angles. (d) GCD curves under different bending angles. (e) Cycle performance of wearable FAZIBs flexed 50 times at each angle at 2.4 A cm^{-3}. (f) Photographs of the FAZIBs woven into clothes on a doll to power a LED. (g) Coupling solar cells, FAZIBs and a micro pressure sensor for energy harvest, storage, and daily usage. (h) Discharge voltage curves of the FAZIBs at different currents after photocharging. (i) Schematic of the VO_2/carbonized cotton fabric pressure sensor attached to a finger. (j) Different bending displacements of the pressure sensor connected to the FAZIB.

electronics in terms of their concurrently high flexibility and high energy density.

In conclusion, we have developed an *in situ* anodic oxidation strategy to prepare 3D hierarchical DVOH@NC as promising binder-free fibrous cathodes for FAZIBs. The 3D triangle-like morphology of the DVOH@NC composite ensures a sufficient contact area between the electrolyte and electrode materials and guarantees a short zinc ion pathway. The oxygen vacancies introduced in DVOH@NC@CNTF can better the electronic conductivity and ionic conductivity, effectively alleviating the electrostatic interaction due to the need for fewer electrons in the formation of the Zn–O bond as compared to the pristine VOH@NC@CNTF and VO@NC@CNTF. And the diffusion barrier for Zn^{2+} is intensely decreased, dramatically enhancing the structural stability of DVOH@NC@CNTF. As a result, DVOH@NC@CNTF delivers an impressive reversible capacity of 711.9 mA h cm^{-3} at 0.3 A cm^{-3} and long-term durability with 4.5% capacity loss after 3000 cycles. More importantly, a prototype quasi-solid-state FAZIB was successfully constructed with outstanding flexibility and prominent weaving capability to demonstrate its practical feasibility, and could be photo-charged *via* solar cells and further power a pressure sensor. Our encouraging results pave the way for designing high-performance flexible vanadium-based cathodes and boost the further development of next-generation wearable AZIBs.

Conflicts of interest

The authors declare no competing financial interest.

Acknowledgements

This work was supported by the National Key R&D Program of China (No. 2017YFA0204800), the Jiangsu Province Youth Fund (BK20220288), the National Natural Science Foundation of China (No. 12174050), and the Fundamental Research Funds for the Central Universities.

References

1 M. Yu, H. Shao, G. Wang, F. Yang, C. Liang, P. Rozier, C. Z. Wang, X. Lu, P. Simon and X. Feng, *Nat. Commun.*, 2020, **9**, 1–9.
2 H. Zhang, Q. Liu, D. Zheng, F. Yang, X. Liu and X. Lu, *Nat. Commun.*, 2021, **12**, 1–8.
3 Z. Zhu, Z. Zheng, F. Zhang, Y. Wu, M. Trzaskowski, R. Maier, M. R. Robinson, J. J. McGrath, P. M. Visscher, N. R. Wray and J. Yang, *Nat. Commun.*, 2018, **9**, 1–12.
4 Y. Zhao, Y. Lu, H. Li, Y. Zhu, Y. Meng, N. Li, D. Wang, F. Jiang, F. Mo, C. Long, Y. Guo, X. Li, Z. Huang, Q. Li, J. C. Ho, J. Fan, M. Sui, F. Chen, W. Zhu, W. Liu and C. Zhi, *Nat. Commun.*, 2022, **13**, 1–12.
5 L. Li, S. Liu, W. Liu, D. Ba, W. Liu, Q. Gui, Y. Chen, Z. Hu, Y. Li and J. Liu, *Nano-Micro Lett.*, 2021, **13**, 1–14.
6 S. Deng, Z. Tie, F. Yue, H. Cao, M. Yao and Z. Niu, *Angew. Chem., Int. Ed.*, 2022, **134**, e202115180.
7 X. Xie, H. Fu, Y. Fang, B. Lu, J. Zhou and S. J. A. E. M. Liang, *Adv. Energy Mater.*, 2022, **12**, 2102393.
8 W. Zuo, W. Zhu, D. Zhao, Y. Sun, Y. Li, J. Liu and X. Lou, *Energy Environ. Sci.*, 2016, **9**, 2881–2891.
9 Y. Wang, C. Wang, Z. Ni, Y. Gu, B. Wang, Z. Guo, Z. Wang, D. Bin, J. Ma and Y. Wang, *J. Mater. Chem. A*, 2021, **9**, 24325–24335.
10 L. Li, Q. Zhang, B. He, R. Pan, Z. Wang, M. Chen, Z. Wang, K. Yin, Y. Yao and L. Wei, *Adv. Mater.*, 2022, **34**, 2104327.
11 Y. Cai, F. Liu, Z. Luo, G. Fang, J. Zhou, A. Pan and S. Liang, *Energy Storage Mater.*, 2018, **13**, 168–174.
12 W. Sun, F. Wang, S. Hou, C. Yang, X. Fan, Z. Ma, T. Gao, F. Han, R. Hu, M. Zhu and C. Wang, *J. Am. Chem. Soc.*, 2017, **139**, 9775–9778.
13 P. He, G. Zhang, X. Liao, M. Yan, X. Xu, Q. An, J. Liu and L. Mai, *Adv. Energy Mater.*, 2018, **8**, 1702463.
14 W. Liang, D. Rao, T. Chen, R. Tang, J. Li and H. Jin, *Angew. Chem.*, 2022, e202207779.
15 M. Yan, P. He, Y. Chen, S. Wang, Q. Wei, K. Zhao, X. Xu, Q. An, Y. Shuang, Y. Shao, K. T. Mueller, L. Mai, J. Liu and J. Yang, *Adv. Mater.*, 2018, **30**, 1703725.
16 M. Huang, X. Wang, X. Liu and L. Mai, *Adv. Mater.*, 2022, **34**, 2105611.
17 Z. Liu, Q. Yang, D. Wang, G. Liang, Y. Zhu, F. Mo, Z. Huang, X. Li, L. Ma, T. Tang, Z. Lu and C. Zhi, *Adv. Energy Mater.*, 2019, **9**, 1902473.
18 J. Liu, C. Guan, C. Zhou, Z. Fan, Q. Ke, G. Zhang, C. Liu and J. J. Wang, *Adv. Mater.*, 2016, **28**, 8732–8739.
19 J. Yang, Q. Zhang, Z. Wang, Z. Wang, L. Kang, M. Qi, M. Chen, W. Liu, W. Gong, W. Lu, P. Shum and L. Wei, *Adv. Energy Mater.*, 2020, **10**, 2001064.
20 Y. Zeng, Y. Han, Y. Zhao, Y. Zeng, M. Yu, Y. Liu, H. Tang, Y. Tong and X. Lu, *Adv. Energy Mater.*, 2015, **5**, 1402176.
21 B. He, Z. Zhou, P. Man, Q. Zhang, C. Li, L. Xie, X. Wang, Q. Li and Y. Yao, *J. Mater. Chem. A*, 2019, **7**, 12979–12986.
22 Q. Li, Z. Yao, E. Lee, Y. Xu, M. M. Thackeray, C. Wolverton, V. P. Dravid and J. Wu, *Nat. Commun.*, 2019, **10**, 1–7.
23 J. Ding, Z. Du, B. Li, L. Wang, S. Wang, Y. Gong and S. Yang, *Adv. Mater.*, 2019, **31**, 1901820.
24 H. Liu, Z. Zhu, Q. Yan, S. Yu, X. He, Y. Chen, R. Zhang, L. Ma, T. Liu, M. Li, R. Lin, Y. Chen, Y. Li, X. Xing, Y. Choi, L. Gao, H. S. Cho, K. An, J. Feng, R. Kostecki, K. Amine, T. Wu, J. Lu, H. L. Xin, S. P. Ong and P. Liu, *Nature*, 2020, **585**, 63–67.
25 X. Li, M. Li, Q. Yang, H. Li, H. Xu, Z. Chai, K. Chen, Z. Liu, Z. Tang, L. Ma, Z. Huang, B. Dong, X. Yin, Q. Huang and C. Zhi, *ACS Nano*, 2020, **14**, 541–551.
26 Y. Tang, X. Li, H. Lv, D. Xie, W. Wang, C. Zhi and H. Li, *Adv. Energy Mater.*, 2020, **10**, 2000892.
27 Y. Liu, Y. Jiang, Z. Hu, J. Peng, W. Lai, D. Wu, S. Zuo, J. Zhang, B. Chen, Z. Dai, Y. Yang, Y. Huang, W. Zhang, W. Zhao, W. Zhang, L. Wang and S. Chou, *Adv. Funct. Mater.*, 2021, **31**, 2008033.
28 L. Yan, C. Zhu, J. Hao, X. Liang, Y. Bai, Q. Hu, B. Tan, B. Liu, X. Zou and B. Xiang, *Adv. Funct. Mater.*, 2021, **31**, 2102693.
29 J. Bao, X. Zhang, B. Fan, J. Zhang, M. Zhou, W. Yang, X. Hu, H. Wang, B. Pan and Y. Xie, *Angew. Chem.*, 2015, **127**, 7507–7512.

30 T. Xiong, Z. G. Yu, H. Wu, Y. Du, Q. Xie, J. Chen, Y. W. Zhang, S. J. Pennycook, W. S. V. Lee and J. Xue, *Adv. Energy Mater.*, 2019, **9**, 1803815.
31 X. Lu, M. Yu, G. Wang, T. Zhai, S. Xie, Y. Ling, Y. Tong and Y. Li, *Adv. Mater.*, 2013, **25**, 267–272.
32 T. Zhou, J. Shen, Z. Wang, J. Liu, R. Hu, L. Ouyang, Y. Feng, H. Liu, Y. Yu and M. Zhu, *Adv. Funct. Mater.*, 2020, **30**, 1909159.
33 W. Ren, H. Zhang, C. Guan and C. Cheng, *Adv. Funct. Mater.*, 2017, **27**, 1702116.
34 D. Chen, M. Lu, B. Wang, R. Chai, L. Li, D. Cai, H. Yang, B. Liu, Y. Zhang and W. Han, *Energy Storage Mater.*, 2021, **35**, 679–686.
35 N. Sa, T. L. Kinnibrugh, H. Wang, G. Sai Gautam, K. W. Chapman, J. T. Vaughey, B. Key, T. T. Fister, J. W. Freeland, D. L. Proffit, P. J. Chupas, G. Ceder, J. G. Bareno, I. D. Bloom and A. K. Burrell, *Chem. Mater.*, 2016, **28**, 2962–2969.
36 K. Zhu, S. Wei, H. Shou, F. Shen, S. Chen, P. Zhang, C. Wang, Y. Cao, X. Guo, M. Luo, H. Zhang, B. Ye, X. Wu, L. He and L. Song, *Nat. Commun.*, 2021, **12**, 1–9.
37 X. Zhu, W. Wang, Z. Cao, S. Gao, M. O. L. Chee, X. Zhang, P. Dong, P. M. Ajayan, M. Ye and J. Shen, *J. Mater. Chem. A*, 2021, **9**, 17994–18005.
38 J. He and A. Manthiram, *Adv. Energy Mater.*, 2020, **10**, 1903241.
39 S. Wei, C. Wang, S. Chen, P. Zhang, K. Zhu, C. Wu, P. Song, W. Wen and L. Song, *Adv. Energy Mater.*, 2020, **10**, 1903712.
40 J. L. Andrews, A. Mukherjee, H. D. Yoo, A. Parija, P. M. Marley, S. Fakra, D. Prendergast, J. Cabana, R. F. Klie and S. Banerjee, *Chem*, 2018, **4**, 564–585.
41 Y. Yang, Y. Tang, G. Fang, L. Shan, J. Guo, W. Zhang, C. Wang, L. Wang, J. Zhou and S. Liang, *Energy Environ. Sci.*, 2018, **11**, 3157–3162.
42 D. Bin, W. Huo, Y. Yuan, J. Huang, Y. Liu, Y. Zhang, F. Dong, Y. Wang and Y. Xia, *Chem*, 2020, **6**, 968–984.
43 J. Zhu, L. Cao, Y. Wu, Y. Gong, Z. Liu, H. E. Hoster, Y. Zhang, S. Zhang, S. Yang, Q. Yan, P. M. Ajayan and R. Vajtai, *Nano Lett.*, 2013, **13**, 5408–5413.
44 L. Ma, H. Yuan, W. Zhang, G. Zhu, Y. Wang, Y. Hu, P. Zhao, R. Chen, T. Chen, J. Liu, Z. Hu and Z. Jin, *Nano Lett.*, 2017, **17**, 7839–7846.
45 C. Ma, J. Alvarado, J. Xu, R. J. Clement, M. Kodur, W. Tong, C. P. Grey and Y. S. Meng, *J. Am. Chem. Soc.*, 2017, **139**, 4835–4845.
46 R. Basu, A. K. Prasad, S. Dhara and A. Das, *J. Phys. Chem. C*, 2016, **120**, 26539–26543.
47 Y. Zeng, Z. Lai, Y. Han, H. Zhang, S. Xie and X. Lu, *Adv. Mater.*, 2018, **30**, 1802396.
48 X. Li, X. Ma, Y. Hou, Z. Zhang, Y. Lu, Z. Huang, G. Liang, M. Li, Q. Yang, J. Ma, N. Li, B. Dong, Q. Huang, F. Chen, J. Fan and C. Zhi, *Joule*, 2021, **5**, 2993–3005.
49 H. Geng, M. Cheng, B. Wang, Y. Yang, Y. Zhang and C. C. Li, *Adv. Funct. Mater.*, 2020, **30**, 1907684.
50 C. Ye, H. Jin, J. Shan, Y. Jiao, H. Li, Q. Gu, K. Davey, H. Wang and S. Z. Qiao, *Nat. Commun.*, 2021, **12**, 1–11.
51 J. Holoubek, Y. Yin, M. Li, M. Yu, Y. S. Meng, P. Liu and Z. Chen, *Angew. Chem.*, 2019, **131**, 19068–19073.
52 Y. Tang, X. Li, H. Lv, W. Wang, Q. Yang, C. Zhi and H. Li, *Angew. Chem.*, 2021, **133**, 5503–5512.
53 G. Fang, J. Zhou, A. Pan and S. Liang, Recent advances in aqueous zinc-ion batteries, *ACS Energy Lett.*, 2018, **3**, 2480–2501.
54 W. Li, C. Han, Q. Gu, S. L. Chou, J. Z. Wang, H. K. Liu and S. X. Dou, *Adv. Energy Mater.*, 2020, **10**, 2001852.
55 F. Cui, D. Wang, F. Hua, X. Yu, C. Guan, G. Song, F. Xu and K. Zhu, *Energy Storage Mater.*, 2022, **44**, 197–205.
56 Y. Liu, X. Hu, J. Li, G. Zhong, J. Yuan, H. Zhan, Y. Tang and Z. Wen, *Nat. Commun.*, 2022, **13**, 1–13.
57 J. Li, N. Luo, F. Wan, S. Zhao, Z. Li, W. Li, J. Guo, P. R. Shearing, D. J. L. Brett, C. J. Carmalt, G. Chai, G. He and I. P. Parkin, *Nanoscale*, 2020, **12**, 20638–20648.
58 M. S. Chae, A. Chakraborty, S. Kunnikuruvan, R. Attias, S. Maddukuri, Y. Gofer, D. T. Major and D. Aurbach, *Adv. Energy Mater.*, 2020, **10**, 2002077.
59 J. Huang, Z. Wang, M. Hou, X. Dong, Y. Liu, Y. Wang and Y. Xia, *Nat. Commun.*, 2018, **9**, 1–8.
60 Z. Guo, Y. Zhao, Y. Ding, X. Dong, L. Chen, J. Cao, C. Wang, Y. Xia, H. Peng and Y. Wang, *Chem*, 2017, **3**, 348.
61 M. Li, J. Meng, Q. Li, M. Huang, X. Liu, K. A. Owusu, Z. Liu and L. Mai, *Adv. Funct. Mater.*, 2018, **28**, 1802016.
62 Y. Zeng, Y. Meng, Z. Lai, X. Zhang, M. Yu, P. Fang, M. Wu, Y. Tong and X. Lu, *Adv. Mater.*, 2017, **29**, 1702698.
63 Q. Yang, A. Chen, C. Li, G. Zou, H. Li and C. Zhi, *Matter*, 2021, **4**, 3146.
64 J. Zhou, J. Cheng, B. Wang, H. Peng and J. Lu, *Energy Environ. Sci.*, 2020, **13**, 1933–1970.

